Article

Comparison of the Soil Water, Vapor, and Heat Dynamics between Summer Maize and Bare Fields in Arid and Semi-Arid Areas

Wande Gao [1,2], Xiuhua Liu [1,2,*], Ce Zheng [1,2,*], Yudong Lu [1,2], Junqi He [1,2] and Yi He [1,2]

[1]   Key Laboratory of Subsurface Hydrology and Ecological Effect in Arid Region of Ministry of Education, Chang'an University, Xi'an 710054, China
[2]   School of Water and Environment, Chang'an University, Xi'an 710054, China
*   Correspondence: liuxh68@chd.edu.cn (X.L.); zhengce@chd.edu.cn (C.Z.)

Abstract: In arid and semi-arid areas, water vapor transport is an important form of soil water movement and plays a crucial role in the overall water and energy balance. For better prediction of soil water and heat fluxes and understanding of root zone soil water dynamics for effective crop management, soil moisture, temperature, soil texture and micrometeorological data have been collected from field trials. Based on the data collected, a Hydrus 1D model was established to simulate the coupled transport of liquid water, water vapor and heat under summer maize (summer maize treatment; SMT) and bare soil (bare soil treatment; BT) for a 100 cm soil profile. Calibration and validation data for the model revealed a good level of agreement between simulated and measured data. Results indicated that the isothermal vapor flux was close to zero throughout the profile, while the isothermal water flux dominated the soil water movement for both SMT and BT. The vapor flux was mainly contributed by thermal vapor flux and increased with soil desiccation. Evaporation and transpiration showed two distinct phases, increasing immediately after irrigation and decreasing gradually as soil water content decreased. SMT had lower evaporation rates due to the protection provided by crop canopy. Irrigation significantly altered the dynamic characteristics of thermal liquid water and thermal vapor fluxes in the vadose, emphasizing the importance of considering the coupled transport of liquid water, vapor, and heat transport at interfaces in the soil–plant–atmosphere continuum for accurate estimates of water flux, especially under prolonged drought conditions.

Keywords: soil heat and water transport; vapor flux; root zone water dynamics; irrigation activity; evapotranspiration

1. Introduction

Irrigation not only increases crop yield but also changes the hydrological cycle [1,2]. It is accepted that forms of soil water movement include both the liquid phase and the vapor phase. In arid and semi-arid areas, due to strong evaporation and large temperature differences between day and night, liquid water and vapor in the soil frequently converse; liquid water evaporates in the form of vapor water, and the vapor condenses into liquid water on the cold surface at night driven by the temperature gradient [3,4]. As the water content of the soil near the surface is typically low, evapotranspiration is a major component of the total water flow and energy balance [4–11]. The distribution of precipitation to surface runoff and infiltration, partitioning and converting net radiation into sensible and latent heat fluxes is also controlled by the soil water content near the soil surface [4,11]. In agricultural applications, soil temperature and soil water content affect crops' growth and development, which are typically grown in certain water and temperature ranges. In addition, soil temperature and moisture influence plant germination, root development and nutrient uptake, as well as soil chemistry, organic matter and nitrogen uptake [12,13].

Investigations into soil water and heat status provide the basis for the efficient utilization of soil water and nutrients and are thus essential to improving soil quality.

Previous research about the interaction of liquid water, vapor and heat transport suggested a link between the movement of soil water content and heat [14]. The guiding equation for liquid water and vapor was derived using Richards' equation [15], which originally only took into account the pressure head gradient for governing isothermal flow. Philip and De Vries [16] expanded Richards' equation to describe the movements of liquid water and vapor within the soil, driven by both the pressure head and the soil temperature gradient (henceforth called the PDV Model). Cass et al. [17] estimated the thermal conductivity enhancement factor for vapor flow and compared different approaches. Nassar and Horton [18] added the influence of osmotic pressure on the flow of vapor and liquid water in PDV models, and Zeng et al. [19] and Zeng et al. [20] established a coupled liquid water, water vapor, air, and heat transport model by considering the influence of airflow on water vapor migration.

Due to the complexity of liquid water, vapor, and thermally coupled flows in unsaturated zones, and difficulties in field measurements, particularly near the soil surface, numerical models have been developed for simulating and analyzing processes through variably saturated soil zones [21]. With the continuous improvement of calculation ability and simulation accuracy, numerical simulation has become a powerful technical tool for examining coupled liquid water, vapor, and thermal transport [9,22–24]. Based on the visual interface of windows, Hydrus-1D [25] is a popular modeling software that is widely used to simulate liquid water, vapor, and heat coupled transport in the water–soil–plant-atmosphere system owing to the flexibility in selecting boundary conditions and soil hydraulic function [9,26].

Although coupled liquid water, vapor, and heat transport in the unsaturated zone have been previously examined [23,24,27], these studies have focused more on the bare fields. To the best of our knowledge, the literature provides little quantitative information regarding the components of water fluxes in cultivated fields, particularly with considering the crop growth process. Therefore, to better understand the coupled liquid water, vapor, and heat transport at the soil–plant–atmosphere interface for accurate estimation of water fluxes, the Jinghuiqu (JHQ) irrigation district was chosen as the study area, considering the growth process of crops and selecting a bare field for comparison. The Hydrus-1D model was used to simulate coupled liquid water, vapor, and heat transport under summer maize treatment (SMT) and bare soil treatment (BT). The aims of this study are: (1) to simulate soil water and temperature regimes for SMT and BT and to examine the impact of crop planting and irrigation on soil temperature regimes, and (2) to analyze the impact of irrigation on the transport of liquid water and water vapor, as well as evaporation and transpiration rates for SMT, and to explore their dynamics related to irrigation activities.

2. Materials and Methods

2.1. Experimental Site and Measurements

2.1.1. Study Site

This experiment was carried out at a long-term experimental site of the JHQ farmland irrigation experimental station (108°54′09″ E, 34°33′36″ N; 419 m above m.s.l.), situated in the middle of the Guanzhong Plain, Shaanxi province, China (Figure 1). Having a typical arid and semi-arid climate, this region has an annual average precipitation of 533 mm (30-year average), of which 50~60% occurs during the growing season (from July to September). The area has an average of 75 precipitation days and a very high average annual potential evaporation of 1212 mm, being almost three times larger than annual precipitation. The average annual temperature is approximately 13.6 °C, with a minimum monthly mean temperature of 0.26 °C in January and a maximum temperature of 27.65 °C in July; the average annual total sunshine duration is 1915 h. The depth of the groundwater table is approximately 16 m [28,29].
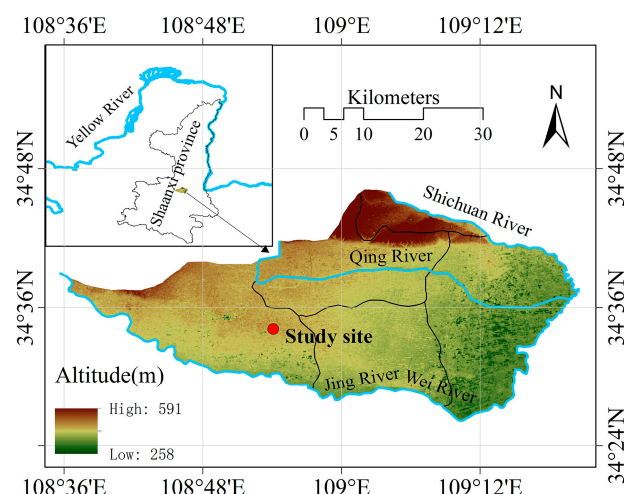
Figure 1. Location of the study site.

2.1.2. Field and Laboratory Measurements

Field experiments were conducted in two adjacent fields at the JHQ in 2013: an abandoned 1953 farmland and a 2200-year-old irrigated and fertilized crop field. For most of recorded history, these actively utilized fields have been in a rotation with maize and winter wheat crops. The irrigation and fertilization practices follow local practices. The total amount of water to be irrigated is about 500 mm per year [28]. The growing season (from sowing to harvest) for summer maize was from the beginning of July to the beginning of October. During a 58-day measurement period from 15 July to 10 September (day of the year (DOY) 196 to 253), rainfall was 89.3 mm. SMT was furrow irrigated twice with surface water (DOY 209 and 234; 100 mm and 210 mm, respectively) and BT without being irrigated. Volumetric soil water content and soil temperature were monitored in situ using Hydra probes connected to a data logger. First, a 100 cm deep hole was dug under SMT and BT, respectively. The probes were installed at soil depths of 10, 20, 40, 70 and 100 cm under SMT and at soil depths of 20, 50, 80, and 100 cm under BT. After all of sensors were installed, the profiles were carefully backfilled. Volumetric soil moisture and temperature were recorded at 10 min and hourly intervals, respectively. In addition, meteorological data, including precipitation, relative humidity, wind speed, and air temperature, were collected from a weather station located in the bare field (Figure 2).

Meanwhile, soil samples (three replications) were collected at corresponding depths for each treatment and were brought back to the laboratory for subsequent analysis. The undisturbed samples were collected by using 100 cm^3 cores and were dried in an oven at 105 °C for 24 h for determination of bulk density. Soil particle size distributions were measured by a Mastersize 2000 instrument (Malvern, Worcestershire WR141XZ, UK) (Table 1). Based on USDA classifications, the soil texture was classified as a silt loam.

Table 1. Soil's physical properties.

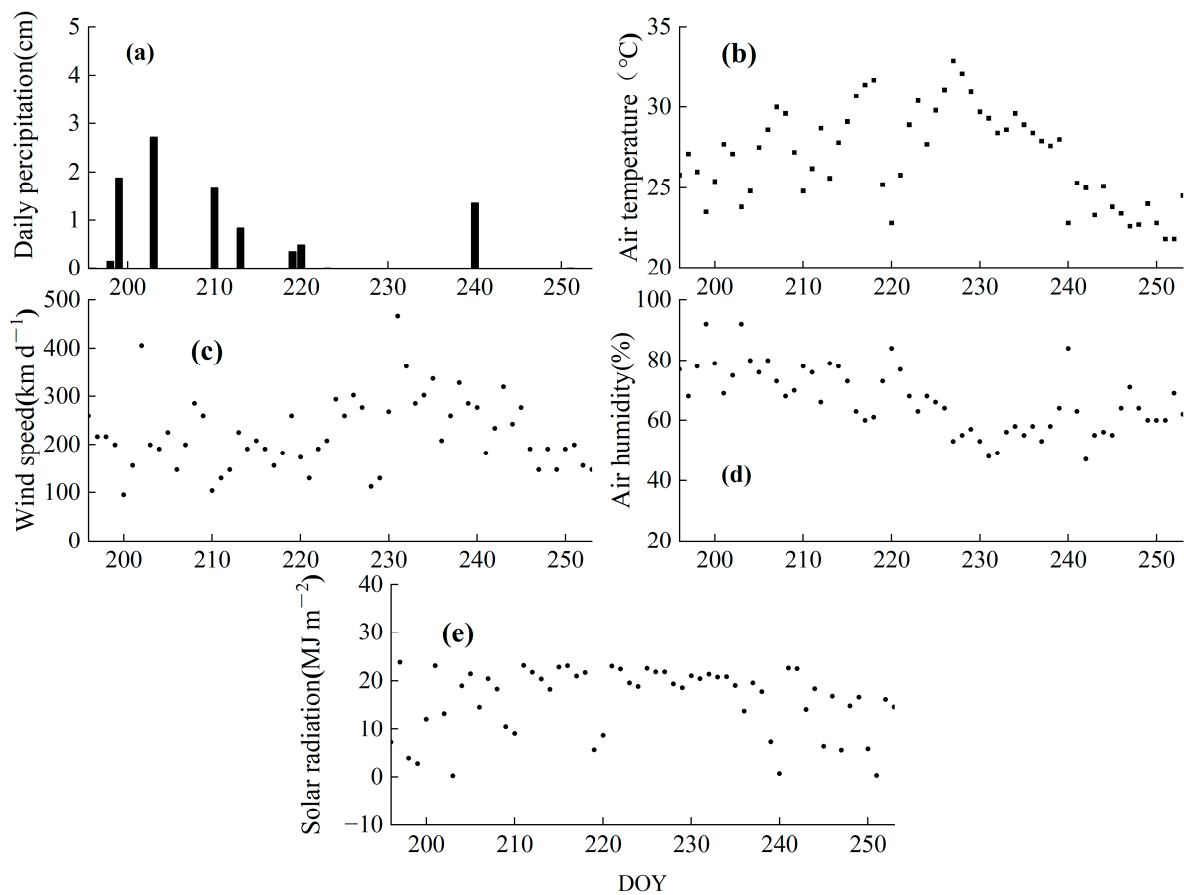| Treatment	Soil Layer (cm)	Particle Size Distribution			Soil Texture	Bulk Density (g cm^{-3})
		Sand (%)	Silt (%)	Clay (%)		
SMT	0–30	10.04	74.89	15.07	Silt Loam	1.55
	30–60	7.63	75.51	16.86	Silt Loam	1.57
	60–100	7.24	75.56	17.20	Silt Loam	1.66
BT	0–30	9.7	74.1	16.2	Silt Loam	1.37
	30–60	3.75	70.95	25.3	Silt Loam	1.54
	60–100	6.85	72.85	20.3	Silt Loam	1.44

Figure 2. Meteorological data during the study period. (**a**) daily precipitation; (**b**) air temperature; (**c**) wind speed; (**d**) air humidity; (**e**) solar radiation.

2.2. Numerical Modeling

2.2.1. Liquid Water and Water Vapor Flow

The numerical model package Hydrus-1D [25] was used to simulate liquid water and water vapor flow coupled with heat transport under field conditions. The governing equation for one-dimensional liquid water and water vapor transport with root water uptake in a variably saturated rigid porous medium can be expressed as in Saito et al., 2006 [9]:

$$\frac{\partial \theta}{\partial t} = \frac{\partial}{\partial z}\left[K_{lh}\frac{\partial h}{\partial z} + K_{lh} + K_{lT}\frac{\partial T}{\partial z} + K_{vh}\frac{\partial h}{\partial z} + K_{vT}\frac{\partial T}{\partial z}\right] - S \tag{1}$$

where θ is total liquid water and water vapor content (cm^3 cm^{-3}); t is time (d); z is the spatial coordinate (cm, positive upward); T is soil temperature (K); h is the matrix potential (cm); K_{lh} (cm d^{-1}) is the isothermal liquid hydraulic conductivity; K_{lT} (cm^2 K^{-1} d^{-1}) is the thermal liquid hydraulic conductivity; K_{vh} (cm d^{-1}) is the isothermal vapor hydraulic conductivity; and K_{vT} (cm^2 K^{-1} d^{-1}) is the thermal vapor hydraulic conductivity; and S is a sink term, referring to root water uptake (d^{-1}), which can be neglected for bare soil treatment in this study.

The van Genuchten model [30] and the pore-size distribution model of Mualem [31] were used to describe the water retention curve and the hydraulic conductivity function (K_{Lh}); thermal hydraulic conductivity (K_{lT}) was described by Noborio et al. [32]; and isothermal vapor hydraulic conductivity (K_{vh}) and thermal vapor hydraulic conductivity (K_{vT}) are described by Nassar and Horton [18] and Saito et al. [9]. A more thorough description of the equation is available in the work of Saito et al. [9].

2.2.2. Soil Heat Transport

The governing equation for heat transport with water flow, vapor flow and heat sink by root water uptake utilized in Hydrus-1D was expressed as in Saito et al., 2006 [9]:

$$\frac{\partial C_p T}{\partial t} + L_0 \frac{\partial \theta_v}{\partial t} = \frac{\partial}{\partial z}\left[\lambda(\theta)\frac{\partial T}{\partial z}\right] - C_w \frac{\partial q_l T}{\partial z} - C_v \frac{\partial q_v T}{\partial z} - L_0 \frac{\partial q_v}{\partial z} - C_w ST \tag{2}$$

where L_0 is the volumetric latent heat of vaporization (J cm^{-3}); C_p, C_w, and C_v are volumetric heat capacities of soil, liquid water and vapor phases (J cm^{-3} K^{-1}), respectively; q_l is liquid water flux densities (cm d^{-1}); q_v is water vapor flux densities (cm d^{-1}); and $\lambda(\theta)$ is the apparent thermal conductivity of the soil (J cm^{-3} d^{-1} K^{-1}).

Thermal conductivity as a function of soil water content is expressed using a non-linear equation, as in Chung and Horton, 1987 [33]:

$$\lambda(\theta) = b_1 + b_2\theta_l + b_3\theta_l^{0.5} \tag{3}$$

where b_1, b_2 and b_3 are empirical parameters (W m^{-1} K^{-1}).

2.2.3. Root Water Uptake Functions

The sink term (S), expressing the volume of water removed per unit time from a unit volume of soil due to plant water uptake, can be calculated according to the Feddes' model [34], as:

$$S(h,z) = \alpha(h)b(z)T_p \tag{4}$$

where $S(h,z)$ is the rate of root water uptake; $\alpha(h)$ is the root water uptake water stress response function (-); $b(z)$ is the normalized water uptake distribution function (cm^{-1}); and T_p is the potential transpiration rate (cm d^{-1}). Parameters for the Feddes' water stress reduction function for corn (summer maize) were selected from the Hydrus internal database (Table 2).

Table 2. Water stress response function parameters used in Hydrus-1D.

Crop	Root Water Uptake Parameters						
	h_0 (cm)	h_{opt} (cm)	h_{2H} (cm)	h_{2L} (cm)	h_3 (cm)	r_{2H} (cm d^{-1})	r_{2L} (cm d^{-1})
Corn	−15	−30	−325	−600	−80,000	0.5	0.1

Note: h_0 (the anaerobiosis point pressure head) is the pressure head below which roots start to extract water from the soil; h_{opt} is the value of the pressure head below which roots extract water at the maximum possible rate; h_{2H} is the value of the limiting pressure head, below which roots can no longer extract water at the maximum rate; and h_{2L} has the same pressure head as h_{2H} with a potential transpiration rate of r_{2L}; h_3 (the wilting point pressure head) is the pressure head below which root-water uptake ceases.

2.2.4. Estimation of Potential *ET*

The Penman–Monteith combination equation [35] was used for calculating the reference crop ET_0. The reference crop ET_0 and the crop coefficient K_C were used to determine the potential crop evapotranspiration (ET_C).

$$ET_C = ET_0 \times K_C \tag{5}$$

For the crop, which only partly covers the soil surface, ET_p is divided into potential evaporation, E_p, and potential transpiration, T_p.

$$E_p = ET_C e^{-kLAI} \tag{6}$$

$$T_p = ET_C - E_p \tag{7}$$

where *k* is the constant for the radiation extinction by crop; the default in Hydrus-1D is 0.463, and *LAI* is the leaf area index.

2.2.5. Initial and Boundary Conditions

A 100 cm soil profile and 1 cm spatial discretization were selected for both SMT and BT, resulting in 101 elements across the 100 cm soil profile. The one-dimensional flow domain was divided into three homogeneous layers (0–30, 30–60, and 60–100 cm) for the two plots. Simulated soil water contents and temperatures were compared with observed values using data from nodes at 20, 40 and 70 cm for SMT and at 20, 50 and 80 cm for BT. The measured soil water contents and temperatures at the start of the simulation were set as the initial conditions at the measured nodes; other nodes were interpolated linearly (between different nodes measured). At the top, the atmospheric flux boundary condition was used due to a lack of bottom flux information and the groundwater table being located far from the interest domain. Free drainage, a zero-gradient boundary condition that can be used to simulate a freely draining soil profile, was used as the boundary condition for the bottom. Surface and 100 cm depth soil temperatures were used as the upper and lower heat boundary conditions [33].

2.2.6. Water Flow and Heat Transport Simulation

Numerical simulations of coupled liquid water, water vapor and heat transport under the two treatments were undertaken from 15 July to 10 September, 2013 (DOY 196 to 253). The model was calibrated from DOY 196 (15 July 2013) to DOY 220 (8 August 2013) using soil water content and soil temperature data at three depths (20, 40, 70 cm for SMT and 20, 50, 80 cm for BT). Results were validated using responding data from DOY 220 (8 August 2013) to DOY 253 (10 September 2013). Using the RETC software package [36], soil hydraulic parameters in the Van Genuchten model [30] were initially obtained by the neural network method (texture percentages (%sand, %silt, %clay) bulk density (BD) as input data). To improve agreement between field measurements and simulated data at different depths, soil hydraulic parameters were additionally optimized by inverse solutions using the non-linear Leven–Berg–Marquardt minimization method [25]. The optimized soil hydraulic parameters for SMT and BT are listed in Table 3.

Table 3. Optimized soil hydraulic parameters for different soil layers.

Treatment	Soil Layer (cm)	θ_r	θ_s	α	n	K_s
SMT	0–30	0.076	0.435	0.012	1.26	13.56
	30–60	0.078	0.44	0.02	1.17	17.2
	60–100	0.083	0.435	0.02	1.17	17.2
BT	0–30	0.089	0.435	0.012	1.26	11.2
	30–60	0.086	0.446	0.011	1.4	15.6
	60–100	0.086	0.446	0.014	1.18	15.6

Note: θ_r, residual water content (cm^3 cm^{-3}); θ_s, saturated water content (cm^3 cm^{-3}); a (cm^{-1}), n (-) are empirical shape parameters; K_s, saturated hydraulic conductivity (cm d^{-1}).

The root-mean-squared error (*RMSE*) and Nash–Sutcliffe efficiency (*NSE*) were used to assess the performance of both calibrated and validated models, defined as:

$$RMSE = \sqrt{\frac{1}{n} \sum_{i=1}^{n} (S_i - O_i)^2} \tag{8}$$

$$NSE = 1 - \frac{\sum_{i=1}^{n} (S_i - O_i)^2}{\sum_{i=1}^{n} (O_i - \overline{O})^2} \tag{9}$$

where *n* is the number of observations; S_i and O_i are the simulated and observed values of soil water content or temperature at time *i*, respectively. $\overline{O}$ is the mean of observed date.

3. Results

3.1. Model Calibration and Validation

Correspondence between observed and simulated soil water contents at the three depths had a good level of fit during calibration and validation periods (Figure 3). An increase in soil water content due to precipitation and irrigation was reasonably predicted by the model, as well as the decrease in soil water content caused by evapotranspiration and redistribution after precipitation and irrigation. It should be noted that soil water content before the second irrigation (DOY 234) at 20 cm and 40 cm depths for SMT were overestimated by the model. This discrepancy may be due to the high heterogeneity in soil properties caused by crop residues and wormholes in the surface layer. Soil properties of heterogeneity were not incorporated into the Hydrus-1D model, and it was assumed that each soil layer was homogeneous during model calibration periods. However, the model simulation of soil water movement did not appear to be significantly affected by this difference.
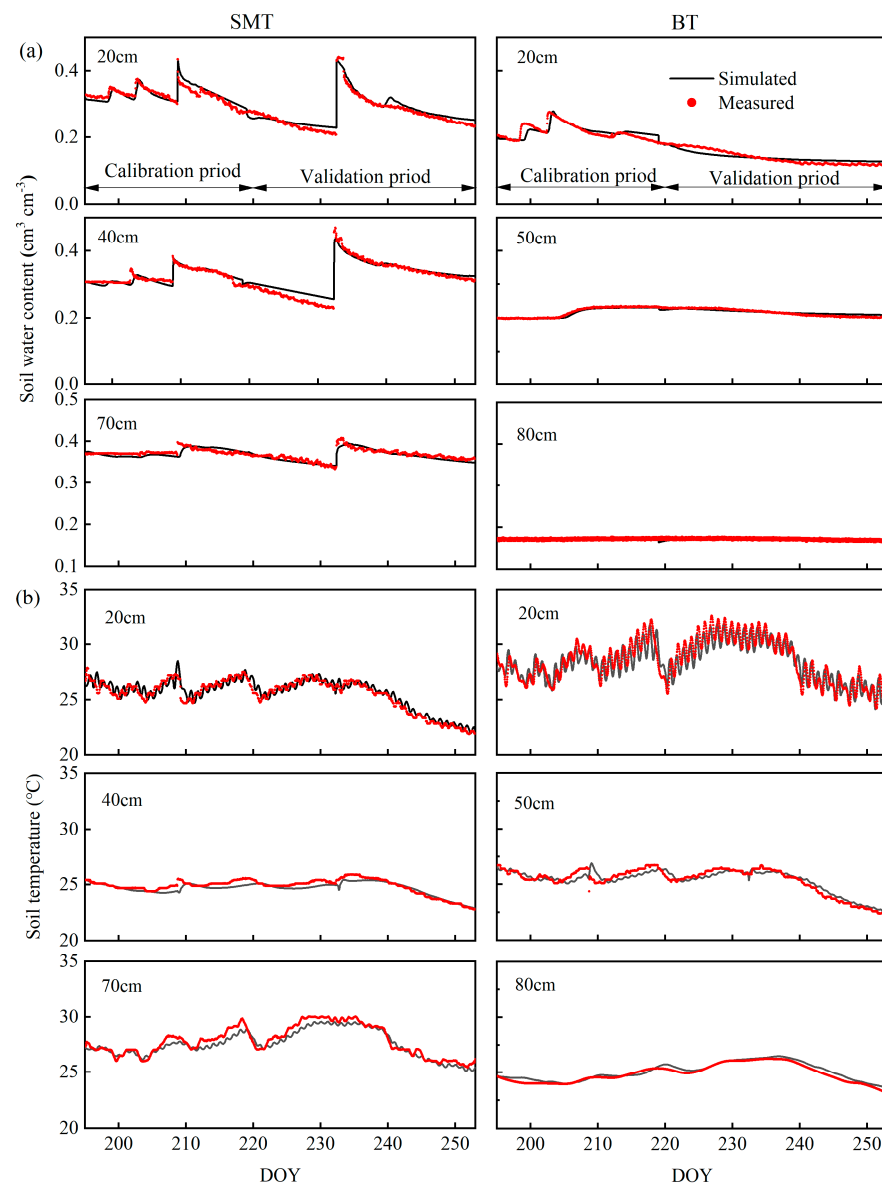

Figure 3. Simulated and measured soil water contents (**a**) and temperature (**b**) at 20, 40 and 70 cm depths for SMT and at 20, 50 and 80 cm depths for BT.

Statistical parameters of quantitative model performance are shown in Table 4. During calibration periods at the three depths, *RMSE* recorded values between 0.008 and 0.014 cm^3 cm^{-3} for SMT and between 0.001 and 0.014 cm^3 cm^{-3} for BT; during validation periods, the values were between 0.006 and 0.015 cm^3 cm^{-3} (SMT) and between 0.002 and 0.01 cm^3 cm^{-3} (BT). At the three sample depths, *NSE* values ranged from −0.618 to 0.749 (SMT) and −0.152 to 0.963 (BT) during calibration periods and between 0.776 to 0.93 (SMT) and −0.12 to 0.788 (BT) during validation periods. These results show that the model had good applicability in the two test plots.

Table 4. Model performance results for simulated soil water contents and temperatures.

Treatment	Soil Depth (cm)	Soil Water Content				Soil Temperature			
		Calibration		Validation		Calibration		Validation	
		RMSE (cm^3 cm^{-3})	*NSE*	*RMSE* (cm^3 cm^{-3})	*NSE*	*RMSE* (°C)	*NSE*	*RMSE* (°C)	*NSE*
SMT	20	0.014	0.641	0.012	0.93	0.588	0.379	0.404	0.939
	40	0.01	0.749	0.015	0.923	0.467	0.077	0.323	0.942
	70	0.008	−0.618	0.006	0.776	0.355	−0.317	0.284	0.888
BT	20	0.014	0.611	0.01	0.788	0.995	0.534	1.064	0.784
	50	0.003	0.963	0.005	0.778	0.524	0.681	0.48	0.907
	80	0.001	−0.152	0.002	−0.12	0.218	0.772	0.272	0.906

Results for variation of simulated and observed soil temperatures in the two treatments at the three depths (Figure 3) recorded good agreement. Compared to the deeper layers in both treatments, soil temperatures recorded significant fluctuations in the upper layer, which can be attributed to the attenuation of transported heat energy. Small *RMSE* values (Table 4) demonstrate that soil temperatures predicted using the Hydrus-1D model were fairly accurate. *RMSE* varied from 0.355 to 0.588 °C for SMT and from 0.218 to 0.995 °C for BT during calibration periods; and from 0.284 to 0.404 °C (SMT) and 0.272 to 1.064 °C (BT) during validation periods. Corresponding *NSE* values ranged from −0.317 to 0.379 (SMT) and 0.534 to 0.772 (BT) during calibration periods and from 0.888 to 0.942 (SMT) and 0.784 to 0.907 (BT) during validation periods at the three depths.

3.2. Liquid Water and Water Vapor during the Select Period

Vertical profiles for isothermal and thermal liquid water and vapor fluxes during a typical period (DOY 208-211, including before and after irrigation at 16:00 h of DOY 209) for SMT are shown in Figure 4. Before irrigation, the isothermal liquid water flux had an upward trend (positive) above 37 cm at 00:00 (on DOY 208) (Figure 4a); below 37 cm, it recorded a downward (negative) trend when the soil water potential gradients changed from upward to downward. The zero-flux plane extended from 37 cm (on DOY 208) to 44 cm (on DOY 209.5) before irrigation. With irrigation on DOY 210, the soil water content and potential in the top-soil layer increased, resulting in a large downward isothermal liquid water flux. Isothermal liquid water fluxes and the soil water potential recorded downward (negative) trends through the soil profile. After irrigation, the isothermal liquid water flux recorded an upward trend above 10 cm on DOY 210.5 as soil near the surface began to dry and above 12 cm on DOY 211 because of the upward gradient of the soil water potential. Furthermore, a very low upward isothermal vapor flux varied from almost zero (no flux) to +0.004 cm d^{-1} above 3 cm was recorded before irrigation (Figure 4b); below 3 cm this could be neglected (1–8 orders lower). After irrigation, however, the isothermal water vapor flux was almost zero across the whole profile and can be neglected.
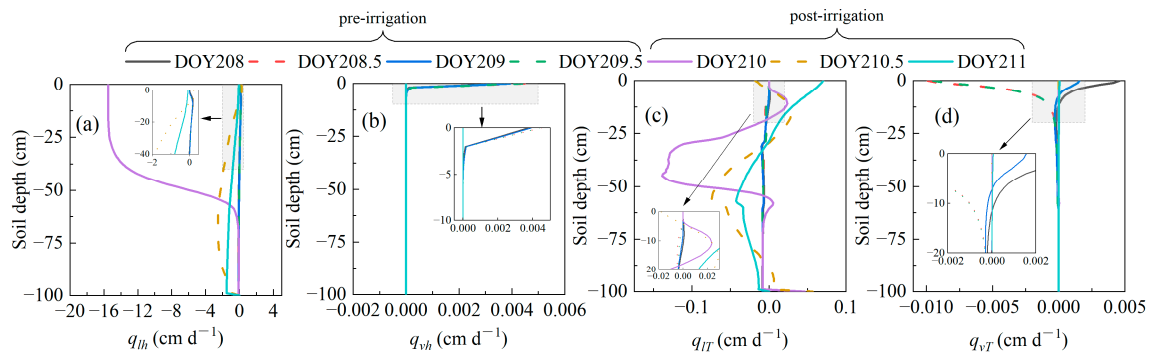
Figure 4. Simulated vertical distributions of the thermal and isothermal fluxes of liquid water and vapor during a typical period from DOY 208 to 211 (27–30 July 2013) before and after an irrigation event for SMT (irrigation starts at 16:00 h and ends at 16:40 h of DOY 209). DOY 208 means 0:00 h of DOY 208; DOY 208.5 means 12:00 h of DOY 208. DOY 208, 208.5, 209 and 209.5 were the pre-irrigation period; DOY 210, 210.5 and 211 were the post-irrigation period. (**a**) The isothermal liquid water flux (q_{lh}); (**b**) the isothermal vapor flux (q_{vh}); (**c**) the thermal liquid water flux (q_{lT}); (**d**) the thermal vapor flux (q_{vT}). All fluxes are positive upward.

Thermal liquid water fluxes recorded a downward (negative) trend below the depth of 11 cm, associated with downward (negative) temperature gradients before irrigation (Figure 4c); above 11 cm, the trend changed from being upward (positive) at nighttime to downward (negative) during the day, closely following changes in the temperature gradient. After irrigation, however, thermal liquid water fluxes recorded noticeable increases (Figure 4c). In comparison, the flux before irrigation could be neglected. In addition, similar to thermal liquid water fluxes, thermal vapor fluxes also recorded the same diurnal variation characteristics near the soil surface.

Vertical profiles of liquid water and vapor fluxes for both isothermal and thermal components during a typical dry period (DOY 244 to 247) for the BT plot were strikingly different (Figure 5). Isothermal liquid water fluxes (Figure 5a) recorded upward (positive) trends throughout the profile, attributed to upward moisture gradients during the selected period. These fluxes were greatest near the surface layers, decreasing rapidly as depth increased. Upward isothermal vapor fluxes (Figure 5b) were also observed but varied only on the order of 10^{-3} to 10^{-7} cm d^{-1} throughout the entire profile, which was almost negligible. In addition, thermal liquid water fluxes (Figure 5c) and vapor fluxes (Figure 5d) recorded downward (negative) trends below 35 cm, associated with downward (negative) temperature gradients from DOY 244 to 247. However, above a depth of 35 cm, thermal liquid water and vapor fluxes exhibit an upward trend during nighttime, associated with upward temperature gradients, and a downward trend during daytime, associated with downward temperature gradients.

In order to further explore the role of vapor and liquid water in the total water dynamic before and after irrigation, as well as during a typical dry period, the quantitative contribution of each component was calculated (Table 5). Over the period of the study, SMT recorded the proportion of total liquid water flux in the whole soil profile to be generally higher than 99.9%, mainly dominated by isothermal liquid water; the maximum vapor water flux was only 0.1% at 2 cm. The isothermal liquid water flux accounted for the largest proportion, followed by the thermal liquid water flux, the thermal vapor flux, and the isothermal vapor flux. These changes were due to a 10 cm irrigation amount applied during this period. During the selected period for BT, the proportion of total liquid water flux across the soil profile ranged from 82.3% to 97.6%, and that of total vapor flux varied from 2.4% to 17.7%. Although water vapor was most significant near the surface layer, the contribution of vapor on water transport gradually decreased with increasing soil depth; even at 100 cm depth, the proportion was still as high as 6.0%, which was higher than that of the thermal liquid water flux. The isothermal liquid water flux accounted for the

largest proportion, followed by the thermal vapor flux, the thermal liquid water flux, and the isothermal vapor flux. Therefore, when investigating soil water transport in shallow soil layers, especially under long-term drought conditions, both vapor and liquid water migration should be considered.
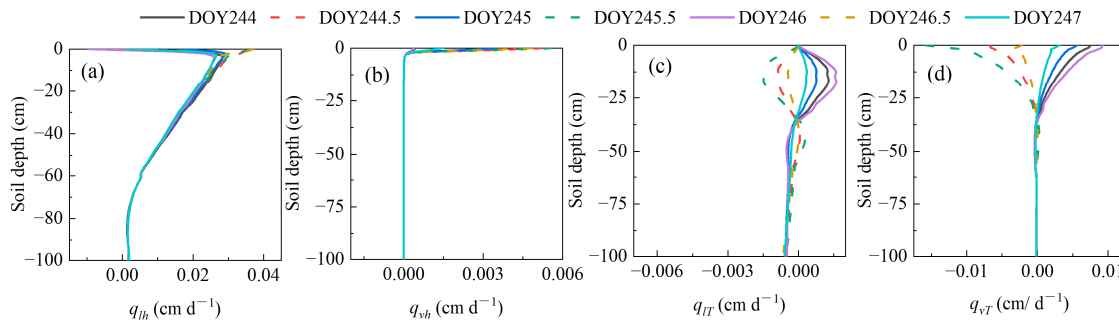

Figure 5. Simulated vertical distributions of the thermal and isothermal fluxes of liquid water and vapor during a typical dry period from DOY 244 to 247 (1–4 September 2013) for BT: (**a**) the isothermal liquid water flux (q_{lh}); (**b**) the isothermal vapor flux (q_{vh}); (**c**) the thermal liquid water flux (q_{lT}); (**d**) the thermal vapor flux(q_{vT}). All fluxes are positive upward.

Table 5. The proportion of each soil water flux component to total flux during a 3-day period before and after irrigation for SMT and a dry period for BT.

Treatment	Soil Depth (cm)	q_{lh}	q_{vh}	q_{lT}	q_{vT}
SMT	2	99.4%	0.0%	0.5%	0.1%
	5	99.6%	0.0%	0.4%	0.0%
	10	99.4%	0.0%	0.6%	0.0%
	20	99.6%	0.0%	0.4%	0.0%
	50	97.7%	0.0%	2.3%	0.0%
	100	98.4%	0.0%	1.6%	0.0%
BT	2	81.9%	0.7%	0.4%	17.0%
	5	84.6%	0.1%	1.5%	13.8%
	10	86.2%	0.0%	3.0%	10.8%
	20	90.2%	0.0%	3.8%	6.0%
	50	94.5%	0.0%	3.1%	2.4%
	100	78.5%	0.0%	15.5%	6.0%

Note: q_{lh}—isothermal liquid fluxes, q_{vh}—isothermal vapor fluxes, q_{lT}—thermal liquid fluxes, q_{vT}—thermal vapor fluxes.

3.3. Evaporation and Transpiration

The rate of evaporation between two successive irrigation events is proportional to the amount of water that is available close to the surface. As shown in Figure 6a, the evaporation under SMT shows two distinct stages. It increased immediately after irrigation (Phase 1) and gradually decreased as soil water content decreased (Phase 2). For example, during DOY 209.5 to 210.5 after irrigation, the evaporation value at Phase 1 increased from 0.0003 to 0.023 cm h^{-1}. After DOY 210.5, evaporation continued to fall off rapidly, and Phase 2 began. This stage was much longer and lasted until the subsequent irrigation. In contrast, no irrigation was carried out at bare soil locations, and most evaporation values were in Phase 2 (Figure 6b). During the simulation period, the average evaporation rates for SMT and BT were 0.0034 and 0.007 cm h^{-1}, respectively. Although irrigations were carried out for SMT, in contrast, the magnitudes of evaporation were much smaller than BT (Figure 6b). This is probably caused by the shading effect of the radiation energy reaching the soil surface in SMT.
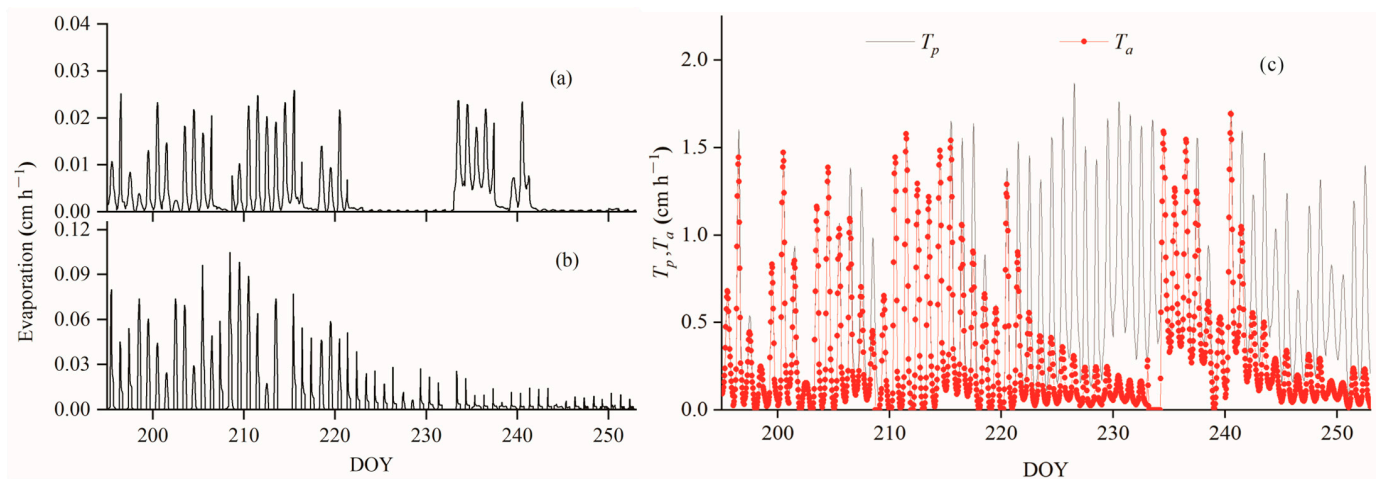
Figure 6. Variation of the evaporation rates for SMT (**a**) and BT (**b**) and simulated potential and actual transpiration rates (T_p and T_a, respectively) for SMT (**c**) during the period from 15 July to 10 September (day of the year (DOY) 196 to 253).

The actual transpiration and potential transpiration rates (T_p and T_a, respectively) were shown in Figure 6c. Simulated actual transpiration and potential varied between 0.00005–1.69 and 0.00006–1.87 cm h^{-1}, respectively. During DOY 195 to 207, the soil water content was relatively high (Figure 3), and the value of T_a was almost equal to the T_p. T_a values also showed two distinct phases, increasing immediately after irrigation (Phase 1) and decreasing gradually as soil water content decreased (Phase 2). The value of T_a was almost the same as T_p at Phase 1 and remained constant for several days (DOY 210–220.5 after the first irrigation or DOY 235–242.5 after the second irrigation). After DOY 220.5 or 242.5, T_a decreased rapidly as the soil dried out and Phase 2 began, indicating that surface soil water was being depleted by root extraction.

3.4. Water Dynamic in the Root Zone

Liquid water, vapor fluxes and their proportions to total water fluxes for SMT and BT are shown in Figures 7 and 8, respectively. Here, liquid water fluxes were the sum of isothermal liquid water fluxes and thermal liquid water fluxes, and water vapor fluxes were the sum of isothermal vapor fluxes and thermal vapor fluxes. Results indicate that liquid water consistently moved upwards during evaporation and crop transpiration at the soil surface, apart from when irrigation or rainfall occurred. Changes in water vapor flux recorded a positive and negative diurnal variation pattern. During the simulation period, irrigation was undertaken twice, and water vapor flux in SMT changed from −0.00322 cm d^{-1} (before the first irrigation) to almost 0 (after the first irrigation) and from 0.002 cm d^{-1} (before the second irrigation) to 0 (after the second irrigation). Corresponding water vapor contribution changed from 3.14% to 0% and 27.37% to 0%, respectively. After irrigation, the water vapor flux was almost zero, and the whole soil profile was dominated by liquid water transport. As the soil dried, water vapor flux and its proportion gradually increased. Similar phenomena were recorded for BT. During the simulation period, the average ratio of water vapor was 3.64% and 8.56%, and the maximum proportion of water vapor was 27.37% and 27.25% at 5 cm under SMT and BT, respectively. The movement of water vapor mainly occurred on the soil surface; as depth increased, the amount and proportion of water vapor decreased.
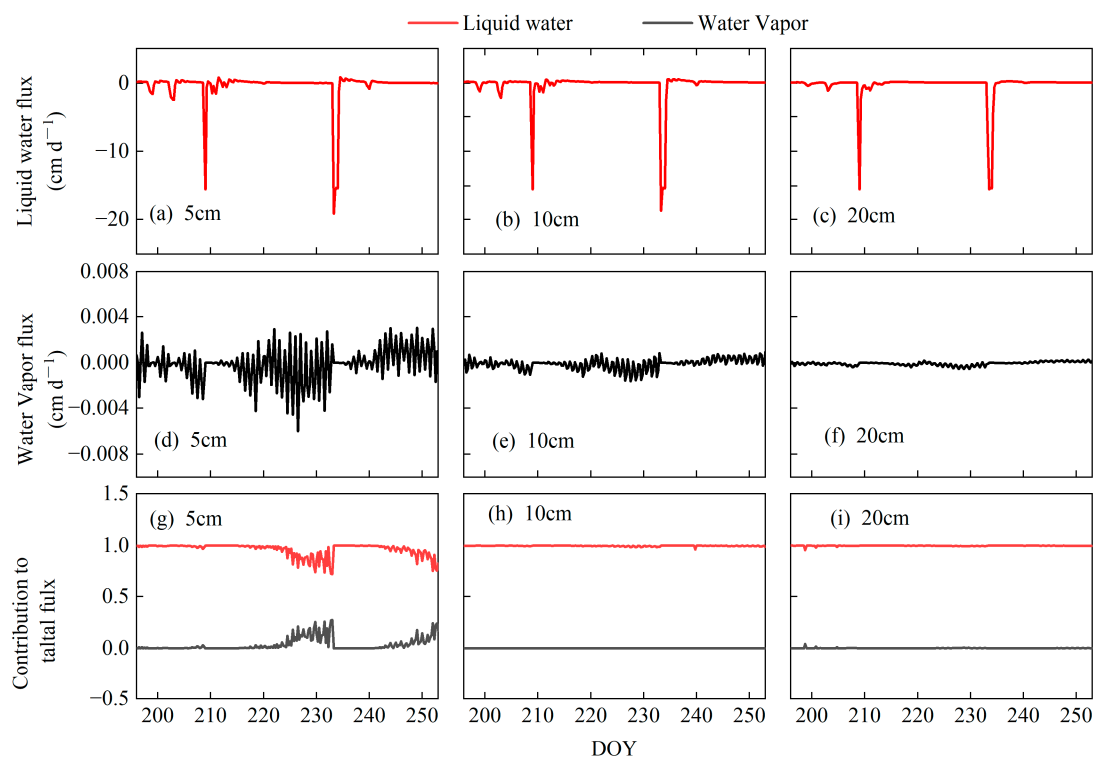
Figure 7. Liquid water and water vapor fluxes and their proportions at 5 cm (**a,d,g**), 10 cm (**b,e,h**) and 20 cm (**c,f,i**) for SMT. All fluxes are positive in the upward direction.
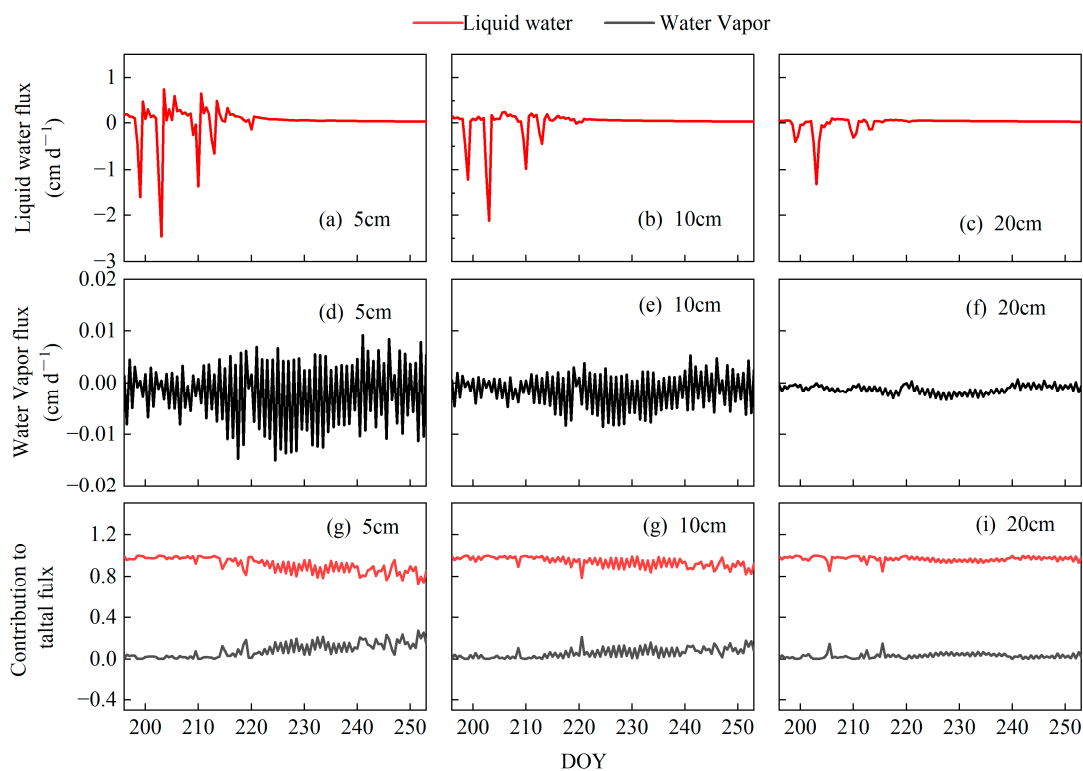

Figure 8. Liquid water and water vapor fluxes and their proportions at 5 cm (**a,d,g**), 10 cm (**b,e,h**) and 20 cm (**c,f,i**) for BT. All fluxes are positive in the upward direction.

For SMT, crop root is mainly distributed in 0–20 cm, which accounts for about 80% of the root distribution according to field measurements. Therefore, water vapor flux

at 5, 10 and 20 cm can represent the variation of water fluxes in the root zone. Liquid water fluxes were the sum of isothermal liquid water fluxes and thermal liquid water fluxes and were determined by water potential gradient, temperature gradient, and the isothermal and thermal hydraulic conductivities for liquid water. From the above results, it can be concluded that the thermal liquid water fluxes account for only a relatively small proportion when the soil is very moist and can be ignored in the case of drought soil conditions (Table 5). Therefore, only isothermal liquid water fluxes were considered. When rainfall or irrigation occurs on the surface, the soil water potential in the root zone increases, and the soil water potential gradient turns downward. Soil water in the root zone moves downward; part is consumed by evaporation, part is consumed by the root water uptake, and part is stored in the soil. Therefore, in the process of soil water infiltration, root water uptake and evaporation affect the root zone water fluxes, as shown in Figure 7a–c. With increasing depth, the water flux in the root zone decreases. Evaporation from the surface and soil water uptake by the roots depleted water in the root zone, causing zone soil drying.

4. Discussion

4.1. Modeling Implications

The Richards equation used to simulate soil water flow involves hydraulic conductivity, pressure head, water content, and boundary conditions. The difficulty of this model lies in the determination of soil moisture characteristic parameters [37]. Soil hydraulic parameters can be estimated by many direct or indirect methods. Direct methods are through small-scale laboratory analysis of soil samples or small-scale field tests, both of which have their own advantages and limitations [38]. The laboratory experiments can measure the soil water retention curve in a wide range and consider the wettest and driest conditions [39]. However, this method requires high equipment and time, which is labor-intensive [40]. The volume of samples analyzed in the laboratory cannot represent the volume of the actual situation in the field [41], and the experimental conditions in the laboratory cannot wholly describe the actual conditions [42]. Therefore, the soil hydraulic parameters obtained from the laboratory analysis of small soil cores are insufficient to simulate the soil water flow on a larger spatial scale [43]. Due to the limitations of direct measurement of soil hydraulic parameters, the ROSETTA pedotransfer function is used to predict soil hydraulic parameters. However, in some cases, the reliability of these relationships is uncertain and needs to be verified in different regions [44].

In the past decades, the application of indirect determination of soil hydraulic parameters by inverse modeling has increased because it can estimate hydraulic properties reasonably from relatively simple data [45–47]. This method estimates a finite set of unknown model parameters by easily measurable variables through an objective function optimization process. The limitation of inversion prediction model parameters is mainly the model uncertainty caused by the non-uniqueness of parameters. The influence of uncertainty of the model can be minimized by taking into account two points. Firstly, the objective function should have a wide range of inversion inputs, such as water content and soil pressure head [48]. Secondly, the initial values of soil parameters should be reasonably close to their actual values [49].

The percentages of sand, silt, and clay are used as input variables of the ROSETTA pedotransfer function to predict the parameters of the van Genuchten–Mualem (VGM) model of soil hydraulic function for SMT and BT, and they are applied as the initial estimated values of inverse model. Compared with the values of hydraulic parameters obtained from previous research in this study area [28], the estimated hydraulic parameters can better represent the soil types in the study area. To improve agreement between field measurements and simulated data at different depths, soil hydraulic parameters were additionally optimized by inverse solutions using the non-linear Leven–Berg–Marquardt minimization method [25]. For SMT, the range of soil moisture change is large. The hydraulic parameters obtained by its inversion are closer to the actual values, which reduces the uncertainty of the model to a certain extent. On the contrary, the soil moisture

only changes in a small range in BT, and the hydraulic parameters optimized by inversion have certain uncertainties. The variation of simulated water and water vapor fluxes is uncertain to some extent, which should be further investigated on the basis of follow-up experience.

4.2. Influence of Irrigation on Water and Vapor Fluxes

Isothermal water flux dominated the soil water movement both for SMT and BT, while the isothermal vapor flux was almost zero throughout the profile, which can be neglected. The vapor flux was mainly contributed by thermal vapor flux and increased with increasing soil desiccation, which was consistent with that of Saito et al. [9], who indicated that the thermal liquid water flux was close to zero on dry days. These findings also indicate that for very wet soils, there was an apparent thermal liquid flux at the soil surface when the soil water diffusivity was not much smaller than the thermal diffusivity [50]. In addition, similar to thermal liquid water fluxes, thermal vapor fluxes also recorded the same diurnal variation characteristics near the soil surface (Figure 4d). However, results indicated that thermal vapor fluxes recorded an obvious decrease after irrigation.

After irrigation, isothermal and thermal vapor fluxes were almost zero, being mainly attributed to two factors: (1) soil water increased and filled in pore spaces between soil particles after irrigation, thereby reducing air-filled pore spaces and not being conducive to water vapor diffusion; (2) temperatures declined and the temperature gradient decreased after irrigation, thereby reducing the thermal vapor flux. Zheng et al. [24] also indicated that increasing soil water and decreasing temperature gradient after rainfall result in a decrease in water vapor.

4.3. Comparison of Water and Temperature Regimes

Compared with BT, irrigation was carried out during the summer maize growth period, resulting in significantly higher soil water contents, coinciding with deep percolation and transpiration (Table 6). In contrast, evaporation values were recorded to have opposite characteristics: evaporation rates in BT were higher due to the bare soil surface; SMT had lower evaporation rates due to protection provided by the crop canopy. Similar results have been reported in the literature. For example, Deb et al. [51] indicated that the mature pecan canopy helps offset evaporative losses by enhancing soil surface drying or depleting soil moisture due to root water extraction.

Table 6. Field water balance (mm) for SMT and BT during simulation periods.

Treatment	*P*	*I*	*DP*	*E*	*T*	Δ*S*
SMT	89.3	310	174.9	50.1	178.9	−42.41
BT	89.3	0	0.1617	104.39	0	−15.27

Note: *P*—precipitation, *I*—irrigation (mm), *DP*—deep percolation, *E*—evaporation, *T*—transpiration, Δ*S*—soil storage.

Compared with SMT, soil water contents at 20 cm from DOY 223 to 253 recorded an obvious diurnal fluctuation phenomenon for BT. This finding was probably due to the upward water vapor migration related to nighttime temperature gradients. Diurnal fluctuations in soil water content similar to those recorded in our investigation have also been previously recorded [52,53].

During this period, soil water near the surface was relatively low, and thermal vapor dominated water vapor transport. During the nighttime, thermal liquid water and water vapor moved from deeper soil layers to the surface under the upward soil temperature gradient. Since latent heat flux during the night was small, the amount of thermal liquid water and water vapor transmitted to the atmosphere through evaporation was minimal. Thermal vapor condensing on cold surfaces and the accumulation of thermal liquid water resulted in increasing nighttime soil water contents. Saito et al. [9] and Bittelli et al. [52] also indicated that thermal vapor condensation and liquid water accumulation near the soil surface increased soil water at night.

Soil temperature changes represent the absorption and emission of soil energy. Soil temperatures for BT were significantly higher, and the temperature amplitude was larger than that of SMT. This phenomenon could be explained by the surface energy balance equation, which effectively describes energy partitioned on the surface. The surface energy balancing components are related heavily to soil water content [54,55]. For soil with higher water content, more energy is partitioned into latent heat flux and attributed to more water available for evaporation [56]; however, at low soil water contents, more energy is partitioned to sensible heat flux and surface heat flux [55]. In addition, crop cultivation was another factor resulting in temperature differences. Crop residues used for mulching are known to reduce soil evaporation and decrease soil temperature and diurnal soil temperature variations [57]. Similarly, Kader et al. [58] reported that mulching treatments protect soils from heat during summer, reducing daily maximum soil temperatures by 1–2 °C compared to bare soil. The planting of summer maize can be regarded as a special kind of surface crop residue, potentially influencing soil hydrothermal characteristics. Thus, with a particular crop covering the soil surface, a considerable portion of daytime solar radiation can be blocked by the crop canopy, reducing energy loss at night and thereby reducing variations in surface temperature. Inversely, because BT had no vegetation cover, it directly received solar radiation, resulting in the surface soil temperature being directly affected by the atmospheric temperature, consistent with atmospheric temperature changes and amplitude.

5. Conclusions

In this study, a Hydrus-1D model was used to simulate coupled liquid water, water vapor and heat transport for soils having a summer maize treatment (SMT) and bare soil treatment (BT). The model was suitably calibrated and verified using observed soil water and temperature data, recording a good fit between simulated and measured data. Owing to two irrigation episodes on the SMT during the growing season, soil water content under SMT was higher than that under BT. However, soil temperature under BT was higher than that under SMT. As a special kind of surface crop residue, summer maize planting combined with soil water affected the hydrothermal characteristics of the soil. During the study period, vapor flux decreased to near zero under SMT, with liquid water transport dominating the whole soil profile after irrigation; the proportion of total liquid water flux in SMT usually increased after irrigation, generally higher than 99.9%. However, the total liquid water flux in the whole soil profile under BT ranged from 82.3% to 97.6%, and the total vapor flux varied from 17.7% to 2.4% during the study period. Water vapor was most substantial near the surface soil layer, becoming important below a certain water content. Our results indicate that, apart from liquid water, vapor also is an important form of the water cycle in natural field vadose zones of arid and semi-arid areas. Therefore, it is important to consider coupled transport of liquid water, vapor and heat to better understand water transport processes, especially in shallow surface layers under long-term drought conditions.

References

1. Li, P.; Ren, L. Evaluating the saline water irrigation schemes using a distributed agro-hydrological model. *J. Hydrol.* **2021**, *594*, 125688. [CrossRef]
2. Nakayama, T. Simulation of the effect of irrigation on the hydrologic cycle in the highly cultivated Yellow River Basin. *Agric. For. Meteorol.* **2011**, *151*, 314–327. [CrossRef]
3. Cahill, A.T.; Parlange, M.B. On water vapor transport in field soils. *Water Resour. Res.* **1998**, *34*, 731–739. [CrossRef]
4. Parlange, M.B.; Cahill, A.T.; Nielsen, D.R.; Hopmans, J.W.; Wendroth, O. Review of heat and water movement in field soils. *Soil Tillage Res.* **1998**, *47*, 5–10. [CrossRef]
5. Gao, W.; Zheng, C.; Liu, X.; Lu, Y.; Chen, Y.; Wei, Y.; Ma, Y. NDVI-based vegetation dynamics and their responses to climate change and human activities from 1982 to 2020: A case study in the Mu Us Sandy Land, China. *Ecol. Indic.* **2022**, *137*, 108745. [CrossRef]
6. Hou, L.; Wang, X.-S.; Hu, B.X.; Shang, J.; Wan, L. Experimental and numerical investigations of soil water balance at the hinterland of the Badain Jaran Desert for groundwater recharge estimation. *J. Hydrol.* **2016**, *540*, 386–396. [CrossRef]
7. Huang, J.; Hou, R.; Yang, H. Diurnal pattern of liquid water and water vapor movement affected by rainfall in a desert soil with a high water table. *Environ. Earth Sci.* **2015**, *75*, 73. [CrossRef]
8. Milly, P.C.D. A Linear Analysis of Thermal Effects on Evaporation From Soil. *Water Resour. Res.* **1984**, *20*, 1075–1085. [CrossRef]
9. Saito, H.; Šimůnek, J.; Mohanty, B.P. Numerical Analysis of Coupled Water, Vapor, and Heat Transport in the Vadose Zone. *Vadose Zone J.* **2006**, *5*, 784–800. [CrossRef]
10. Scanlon, B.R.; Keese, K.; Reedy, R.C.; Simunek, J.; Andraski, B.J. Variations in flow and transport in thick desert vadose zones in response to paleoclimatic forcing (0-90 kyr): Field measurements, modeling, and uncertainties. *Water Resour. Res.* **2003**, *39*, 1179. [CrossRef]
11. Schelde, K.; Thomsen, A.; Heidmann, T.; Schjønning, P.; Jansson, P.E. Diurnal fluctuations of water and heat flows in a bare soil. *Water Resour. Res.* **1998**, *34*, 2919–2929. [CrossRef]
12. Gomez-Rey, M.X.; Couto-Vazquez, A.; Gonzalez-Prieto, S.J. Nitrogen transformation rates and nutrient availability under conventional plough and conservation tillage. *Soil Tillage Res.* **2012**, *124*, 144–152. [CrossRef]
13. Sharratt, B.S.; Gesch, R.W. Emergence of Polymer-Coated Corn and Soybean Influenced by Tillage and Sowing Date. *Agron. J.* **2008**, *100*, 585–590. [CrossRef]
14. Taylor, S.A.; Cavazza, L. The Movement of Soil Moisture in Response to Temperature Gradients1. *Soil Sci. Soc. Am. J.* **1954**, *18*, 351–358. [CrossRef]
15. Richards, L.A. Capillary Conduction of Liquids through Porous Mediums. *Physics* **1931**, *1*, 318–333. [CrossRef]
16. Philip, J.R.; De Vries, D.A. Moisture movement in porous materials under temperature gradients. *Trans. Am. Geophys. Union* **1957**, *38*, 222–232. [CrossRef]
17. Cass, A.; Campbell, G.S.; Jones, T.L. Enhancement of Thermal Water Vapor Diffusion in Soil. *Soil Sci. Soc. Am. J.* **1984**, *48*, 25–32. [CrossRef]
18. Nassar, I.N.; Horton, R. Water Transport in Unsaturated Nonisothermal Salty Soil: II. Theoretical Development. *Soil Sci. Soc. Am. J.* **1989**, *53*, 1330–1337. [CrossRef]
19. Zeng, Y.; Su, Z.; Wan, L.; Wen, J. Numerical analysis of air-water-heat flow in unsaturated soil: Is it necessary to consider airflow in land surface models? *J. Geophys. Res.* **2011**, *116*, D20107. [CrossRef]
20. Zeng, Y.; Su, Z.; Wan, L.; Wen, J. A simulation analysis of the advective effect on evaporation using a two-phase heat and mass flow model. *Water Resour. Res.* **2011**, *47*, W10529. [CrossRef]
21. Antonopoulos, V.Z. Water Movement and Heat Transfer Simulations in a Soil under Ryegrass. *Biosyst. Eng.* **2006**, *95*, 127–138. [CrossRef]
22. Dahiya, R.; Ingwersen, J.; Streck, T. The effect of mulching and tillage on the water and temperature regimes of a loess soil: Experimental findings and modeling. *Soil Tillage Res.* **2007**, *96*, 52–63. [CrossRef]
23. Kader, M.A.; Nakamura, K.; Senge, M.; Mojid, M.A.; Kawashima, S. Numerical simulation of water- and heat-flow regimes of mulched soil in rain-fed soybean field in central Japan. *Soil Tillage Res.* **2019**, *191*, 142–155. [CrossRef]
24. Zheng, C.; Šimůnek, J.; Lu, Y.; Liu, X.; Shi, C.; Li, H. Monitoring and modeling the coupled movement of water, vapor, and energy in arid areas. *J. Hydrol.* **2020**, *590*, 125528. [CrossRef]
25. Šimůnek, J.; Šejna, M.; Saito, H.; Sakai, M.; Van Genuchten, M.T. *The HYDRUS-1D Software Package for Simulating the Movement of Water, Heat, and Multiple Solutes in Variably Saturated Media. Version 4.17, HYDRUS Software Series 3*; Department of Environmental Sciences, University of California Riverside: Riverside, CA, USA, 2013.
26. Zhao, Y.; Peth, S.; Horn, R.; Krümmelbein, J.; Ketzer, B.; Gao, Y.; Doerner, J.; Bernhofer, C.; Peng, X. Modeling grazing effects on coupled water and heat fluxes in Inner Mongolia grassland. *Soil Tillage Res.* **2010**, *109*, 75–86. [CrossRef]
27. Du, C.; Yu, J.; Wang, P.; Zhang, Y. Analysing the mechanisms of soil water and vapour transport in the desert vadose zone of the extremely arid region of northern China. *J. Hydrol.* **2018**, *558*, 592–606. [CrossRef]
28. Liu, X.; Gao, W.; Sun, S.; Hu, A.; He, Y.; He, S.S. Responses of soil water dynamic processes and groundwater recharge to irrigation intensity and antecedent moisture in the vadose zone. *Hydrol. Process.* **2019**, *33*, 849–863. [CrossRef]

29. Liu, X.; Guo, C.; He, S.; Zhu, H.; Li, J.; Yu, Z.; Qi, Y.; He, J.; Zhang, J.; Müller, C. Divergent gross nitrogen transformation paths in the topsoil and subsoil between abandoned and agricultural cultivation land in irrigated areas. *Sci. Total Environ.* **2020**, *716*, 137148. [CrossRef] [PubMed]

30. Van Genuchten, M.T. A Closed-form Equation for Predicting the Hydraulic Conductivity of Unsaturated Soils. *Soil Sci. Soc. Am. J.* **1980**, *44*, 892–898. [CrossRef]

31. Mualem, Y. A new model for predicting the hydraulic conductivity of unsaturated porous media. *Water Resour. Res.* **1976**, *12*, 513–522. [CrossRef]

32. Noborio, K.; McInnes, K.J.; Heilman, J.L. Two-Dimensional Model for Water, Heat, and Solute Transport in Furrow-Irrigated Soil: II. Field Evaluation. *Soil Sci. Soc. Am. J.* **1996**, *60*, 1010–1021. [CrossRef]

33. Chung, S.-O.; Horton, R. Soil heat and water flow with a partial surface mulch. *Water Resour. Res.* **1987**, *23*, 2175–2186. [CrossRef]

34. Feddes, R.A.; Kowalik, P.J.; Zaradny, H. *Simulation of Field Water Use and Crop Yield*; John Wiley & Sons: New York, NY, USA, 1978.

35. Allen, R.G.; Pereira, L.S.; Raes, D.; Smith, M. *Crop Evapotranspiration. Guidelines for Computing Crop Water Requirements, FAO Irrigation and Drainage Paper 56*; Food and Agriculture Organization of the United Nations: Rome, Italy, 1998.

36. Van Genuchten, M.T.; Leij, F.J.; Yates, S.R. *The RETC Code for Quantifying the Hydraulic Functions of Unsaturated Soils*; USA Salinity Laboratory, USDA, ARS: Riverside, CA, USA, 1991.

37. Le Bourgeois, O.; Bouvier, C.; Brunet, P.; Ayral, P.A. Inverse modeling of soil water content to estimate the hydraulic properties of a shallow soil and the associated weathered bedrock. *J. Hydrol.* **2016**, *541*, 116–126. [CrossRef]

38. Ket, P.; Oeurng, C.; Degré, A. Estimating Soil Water Retention Curve by Inverse Modelling from Combination of In Situ Dynamic Soil Water Content and Soil Potential Data. *Soil Syst.* **2018**, *2*, 55. [CrossRef]

39. Asgarzadeh, H.; Mosaddeghi, M.R.; Dexter, A.R.; Mahboubi, A.A.; Neyshabouri, M.R. Determination of soil available water for plants: Consistency between laboratory and field measurements. *Geoderma* **2014**, *226–227*, 8–20. [CrossRef]

40. Scharnagl, B.; Vrugt, J.A.; Vereecken, H.; Herbst, M. Inverse modelling of in situ soil water dynamics: Investigating the effect of different prior distributions of the soil hydraulic parameters. *Hydrol. Earth Syst. Sci.* **2011**, *15*, 3043–3059. [CrossRef]

41. Mallants, D.; Mohanty, B.P.; Vervoort, A.; Feyen, J. Spatial analysis of saturated hydraulic conductivity in a soil with macropores. *Soil Technol.* **1997**, *10*, 115–131. [CrossRef]

42. Basile, A.; Ciollaro, G.; Coppola, A. Hysteresis in soil water characteristics as a key to interpreting comparisons of laboratory and field measured hydraulic properties. *Water Resour. Res.* **2003**, *39*, 1355. [CrossRef]

43. Baroni, G.; Facchi, A.; Gandolfi, C.; Ortuani, B.; Horeschi, D.; van Dam, J.C. Uncertainty in the determination of soil hydraulic parameters and its influence on the performance of two hydrological models of different complexity. *Hydrol. Earth Syst. Sci.* **2010**, *14*, 251–270. [CrossRef]

44. Werisch, S.; Grundmann, J.; Al-Dhuhli, H.; Algharibi, E.; Lennartz, F. Multiobjective parameter estimation of hydraulic properties for a sandy soil in Oman. *Environ. Earth Sci.* **2014**, *72*, 4935–4956. [CrossRef]

45. Pinheiro, E.A.R.; de Jong van Lier, Q.; Inforsato, L.; Šimůnek, J. Measuring full-range soil hydraulic properties for the prediction of crop water availability using gamma-ray attenuation and inverse modeling. *Agric. Water Manag.* **2019**, *216*, 294–305. [CrossRef]

46. Brunetti, G.; Šimůnek, J.; Bogena, H.; Baatz, R.; Huisman, J.A.; Dahlke, H.; Vereecken, H. On the Information Content of Cosmic-Ray Neutron Data in the Inverse Estimation of Soil Hydraulic Properties. *Vadose Zone J.* **2019**, *18*, 1–24. [CrossRef]

47. Schelle, H.; Durner, W.; Iden, S.C.; Fank, J. Simultaneous Estimation of Soil Hydraulic and Root Distribution Parameters from Lysimeter Data by Inverse Modeling. *Proc. Environ. Sci.* **2013**, *19*, 564–573. [CrossRef]

48. Eching, S.O.; Hopmans, J.W. Optimization of Hydraulic Functions from Transient Outflow and Soil Water Pressure Data. *Soil Sci. Soc. Am. J.* **1993**, *57*, 1167–1175. [CrossRef]

49. Kool, J.B.; Parker, J.C.; van Genuchten, M.T. Determining Soil Hydraulic Properties from One-step Outflow Experiments by Parameter Estimation: I. Theory and Numerical Studies. *Soil Sci. Soc. Am. J.* **1985**, *49*, 1348–1354. [CrossRef]

50. Milly, P.C.D. A Simulation Analysis of Thermal Effects on Evaporation From Soil. *Water Resour. Res.* **1984**, *20*, 1087–1098. [CrossRef]

51. Deb, S.K.; Shukla, M.K.; Mexal, J.G. Numerical Modeling of Water Fluxes in the Root Zone of a Mature Pecan Orchard. *Soil Sci. Soc. Am. J.* **2011**, *75*, 1667–1680. [CrossRef]

52. Bittelli, M.; Ventura, F.; Campbell, G.S.; Snyder, R.L.; Gallegati, F.; Pisa, P.R. Coupling of heat, water vapor, and liquid water fluxes to compute evaporation in bare soils. *J. Hydrol.* **2008**, *362*, 191–205. [CrossRef]

53. Jackson, R.D. Diurnal changes in soil water content during drying. In *Field Soil Water Regime*; Bruce, R.R., Ed.; Soil Science Society of America: Madison, WI, USA, 1973.

54. Enz, J.W.; Brun, L.J.; Larsen, J.K. Evaporation and energy balance for bare and stubble covered soil. *Agric. For. Meteorol.* **1988**, *43*, 59–70. [CrossRef]

55. Horton, R.; Bristow, K.L.; Kluitenberg, G.J.; Sauer, T.J. Crop residue effects on surface radiation and energy balance—Review. *Theor. Appl. Climatol.* **1996**, *54*, 27–37. [CrossRef]

56. Heitman, J.L.; Xiao, X.; Horton, R.; Sauer, T.J. Sensible heat measurements indicating depth and magnitude of subsurface soil water evaporation. *Water Resour. Res.* **2008**, *44*, W00D05. [CrossRef]

57. Bristow, K.L.; Campbell, G.S.; Papendick, R.I.; Elliott, L.F. Simulation of heat and moisture transfer through a surface residue—Soil system. *Agric. For. Meteorol.* **1986**, *36*, 193–214. [CrossRef]

58. Kader, M.A.; Senge, M.; Mojid, M.A.; Nakamura, K. Mulching type-induced soil moisture and temperature regimes and water use efficiency of soybean under rain-fed condition in central Japan. *Int. Soil Water Conserv. Res.* **2017**, *5*, 302–308. [CrossRef]